PUBLISHED VERSION

Shtern, V. N.; Mi, Jianchun
Hysteresis and precession of a swirling jet normal to a wall Physical Review E, 2004; 69(1):016312

©2004 American Physical Society

http://link.aps.org/doi/10.1103/PhysRevE.69.016312

PERMISSIONS

http://publish.aps.org/authors/transfer-of-copyright-agreement

"The author(s), and in the case of a Work Made For Hire, as defined in the U.S. Copyright Act, 17 U.S.C.

§101, the employer named [below], shall have the following rights (the "Author Rights"):

[...]

3. The right to use all or part of the Article, including the APS-prepared version without revision or modification, on the author(s)' web home page or employer's website and to make copies of all or part of the Article, including the APS-prepared version without revision or modification, for the author(s)' and/or the employer's use for educational or research purposes."

24th April 2013

http://hdl.handle.net/2440/2886

Hysteresis and precession of a swirling jet normal to a wall

V. Shtern
Department of Mechanical Engineering, University of Houston, Houston, Texas USA

J. Mi
School of Mechanical Engineering, University of Adelaide, SA 5005, Australia
(Received 15 May 2003; published 30 January 2004)

Interaction of a swirling jet with a no-slip surface has striking features of fundamental and practical interest. Different flow states and transitions among them occur at the same conditions in combustors, vortex tubes, and tornadoes. The jet axis can undergo precession and bending in combustors; this precession enhances large-scale mixing and reduces emissions of NO_x. To explore the mechanisms of these phenomena, we address conically similar swirling jets normal to a wall. In addition to the Serrin model of tornadolike flows, a new model is developed where the flow is singularity free on the axis. New analytical and numerical solutions of the Navier–Stokes equations explain occurrence of multiple states and show that hysteresis is a common feature of wall-normal vortices or swirling jets no matter where sources of motion are located. Then we study the jet stability with the aid of a new approach accounting for deceleration and nonparallelism of the base flow. An appropriate transformation of variables reduces the stability problem for this strongly nonparallel flow to a set of ordinary differential equations. A particular flow whose stability is studied in detail is a half-line vortex normal to a rigid plane—a model of a tornado and of a swirling jet issuing from a nozzle in a combustor. Helical counter-rotating disturbances appear to be first growing as Reynolds number increases. Disturbance frequency changes its sign along the neutral curve while the wave number remains positive. Short disturbance waves propagate downstream and long waves propagate upstream. This helical instability causes bending of the vortex axis and its precession—the effects observed in technological flows and in tornadoes.

DOI: 10.1103/PhysRevE.69.016312 PACS number(s): 47.90.+a, 47.20.−k

I. INTRODUCTION

The axis of a swirling jet can undergo precession and bending observed, e.g., in tornadoes and in combustors. Combustors typically include a pipe followed by a large suddenly expanded chamber. The flow issuing from the pipe forms a swirl-free or swirling jet in the chamber. This confined flow has two stable states at the same values of control parameters [1]: in the first state, the jet propagates along the chamber axis while in the second state, the jet rotates gyroscopically around the axis, i.e., precesses. This precession is a favorable feature of burner applications in, e.g., cement and glass kilns, because it enhances large-scale mixing and thereby delivers a significant reduction in emissions of NO_x [2]. Better understanding of the precession formation and multiple-flow-state mechanisms should help us to optimize burner characteristics for minimizing harmful emissions.

To explain the development of precession, we model the axisymmetric flow state by a conical similarity solution of the Navier–Stokes equations and then apply a new stability approach accounting for the base-flow deceleration and streamline divergence downstream. A model flow is a jet issuing into a half-space from a point source on a no-slip plane. That is, we do not consider the flow from the pipe and instead replace the pipe with the point source. Also, we neglect the sidewall of the combustor chamber, i.e., consider the flow in the region whose radial extent is small (large) compared with the diameter of the chamber (pipe). It is shown that the interaction of the jet and the normal wall is itself sufficient to induce precession.

The jet axis in the model is a normal-to-plane half-line vortex singularity of a given circulation (characterized by the swirl Reynolds number Re_s, which is the ratio of the maximum circulation to viscosity) and a given force acting along the axis. Taylor [3], Goldshtik [4], and Serrin [5] studied this flow for different applications such as a fuel atomizer, a vortex nuclear reactor, and a tornado (see review by Shtern and Hussain [6] for details). A striking feature of this model is the solution loss as Re_s increases and reaches a rather small threshold value.

The solution disappearance via the development of a singularity seems paradoxical and even contradictory for a viscous flow. For example, Taylor [3] found a boundary-layer solution which is valid for large Re_s, while Goldshtik [4] proved that the solution does not exist for $\mathrm{Re}_s > 8$ (!), and Guilloud *et al.* [7] calculated the exact value, $\mathrm{Re}_{co} = 5.53$, at which this solution collapses. Goldshtik and Shtern [8] showed that a strong near-axis jet develops and the maximum velocity of this jet tends to infinity as Re_s approaches Re_{co}. One would expect singularities to occur in the limit as $\mathrm{Re}_s \to \infty$, but not at a finite value. Note that all these results were obtained for a vortex with no axial force.

Serrin [5] explored this intriguing feature in a broader context. He applied the vortex-wall model to tornadoes and generalized the problem (in order to avoid the collapse) by introducing an additional source of motion—force $F_z = 4\pi\rho\nu^2 r^{-1} A$ acting along the axis. Here A is a dimensionless characteristic of the force strength per unit length, ρ is the density, ν is the kinematic viscosity, and r is the distance from the jet origin. Figure 1 shows a schematic of this half-line vortex, a typical streamline, and spherical coordinates. Figure 2 is a map of the flow patterns (the insets show the

 ©2004 The American Physical Society

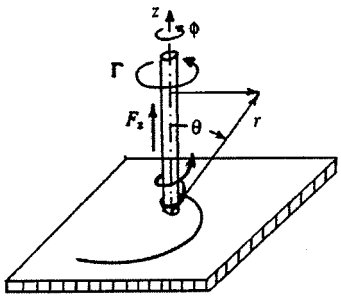

FIG. 1. Flow schematics and coordinates.

meridional motion) on the parameter plane, $k=\mathrm{Re}_s/2$ and $P=1+4A\,\mathrm{Re}_s^{-2}$ [5].

Serrin [5] proved that the solution exists for arbitrarily large Re_s, provided A is properly chosen. However, the collapse paradox remained unresolved because such a solution describes a descending flow (inset A) or a two-cell flow (B), but not an ascending flow (C): There is no solution to the right of curve F and line Co in Fig. 2. Serrin mentioned that he had failed to prove the uniqueness theorem for the entire parameter region where the solution exists. Numerical simulations by Goldshtik and Shtern [8] revealed that the problem has more than one solution: F is a fold curve where two regular solutions merge and disappear. They also showed that collapse occurs along line Co, described by $k^{-2}=0.131P$.

Thus, there are two different mechanisms of the solution loss, i.e., collapse and fold, and only one (collapse) corresponds to the singularity development. Both these mathematical features correspond to physical effects typical of swirling flows: (a) strong accumulation of the axial momentum, e.g., occurring in tornadoes [9], (b) multiple flow states, e.g., observed in vortex chambers [10], and (c) hysteretic transitions among different flow states [11].

All these effects are related to flow stability to infinitesimal and finite-amplitude disturbances. Shtern and Drazin [12] demonstrated a clear relation between stability and hysteresis/folds in a tornado model. Their study, however, was limited to disturbances without time oscillations. Recently, Shtern and Hussain [13] developed a more efficient stability approach that addresses generic disturbances (i.e., including time oscillating). An important advantage of this approach is that it accounts for deceleration and nonparallelism of conical flows and uses neither the parallel flow nor the boundary layer approximations. This advantage helped to find new instabilities missed by previous studies and to correct previous instability results (critical Reynolds numbers appeared to be significantly smaller).

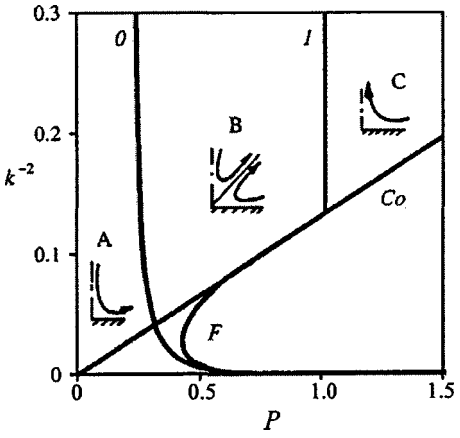

FIG. 2. Map of the flow states in the Serrin model, k is proportional to the swirl Reynolds number and P characterizes the axial force.

Here we extend this nonparallel stability technique to the vortex-wall problem where a singularity is located on the symmetry axis (e.g., in the Serrin vortex). This allows us to explore whether the flow becomes unstable before Re_s reaches its collapse value. As shown below, not only the instability indeed occurs, but also its presence results in bending and precession of the jet axis.

In the reminder of this paper, we first explore hysteresis in models of the vortex-wall flow with and without a singularity on the axis (Sec. II), then describe the stability approach (Sec. III), study the instability of the Serrin flow (Sec. IV), and finally make concluding remarks (Sec. V).

II. HYSTERESIS

Before studying the stability of a swirling jet normal to a wall, we address here some important features of the base flow, e.g., multiple steady states and hysteretic transitions among them, as control parameters vary. As mentioned in Introduction, these features are typical of swirling flows. In addition to the examples in Sec. I, hysteretic transitions are observed above delta-wing aircraft [14] and in diverging vortex tubes [15]. The most relevant for the present study are hysteretic phenomena occurring in tornadoes [16] and in precessing jet nozzle chambers [1].

Since hysteresis is a strongly nonlinear effect, its analysis is a challenge for theoretical and, especially, analytical studies. In this respect, modelling of practical swirling flows by conical similarity solutions is beneficial, because it reduces the Navier–Stokes equations to ordinary differential ones, thus radically easing the analysis. Next, exploiting the fact that hysteresis occurs only when Re_s exceeds a threshold, asymptotic techniques as $\mathrm{Re}_s\to\infty$ can be applied resulting sometimes in analytical solutions. These solutions help to find multiple (e.g., five [11]) steady flow states occurring at the same values of control parameters and to explain hysteretic transitions among them.

Unfortunately, previous studies of hysteresis in conical flows have been limited to swirling jets located far away from no-slip boundaries, while modelling of vortex precession requires accounting for effects of a no-slip wall. One objective of the present study is to fill this gap. In this section, we consider two models of swirling flows near a no-slip boundary: the first one is the Serrin vortex having the strong singularity on the symmetry axis and the second is a new model with a weak singularity located on a conical surface away from both the axis and the wall. We will show below that multiple flow states and folds occur in both problems.

A. Hysteresis in the Serrin flow

The problem on swirling jets has no analytical solution, except for some limiting cases. For this reason, together with integration of the stability equations, we need also to numerically solve the base-flow equations described below. For a conically similar flow, velocity has the representation,

$$v_r = -\nu r^{-1}\psi', \quad v_\theta = -\nu(r\sin\theta)^{-1}\psi,$$

$$v_\phi = -\nu(r\sin\theta)^{-1}\Gamma_b(x), \quad \Psi = \nu r\psi(x), \tag{1}$$

where $\{r,\theta,\phi\}$ are spherical coordinates, r is the distance from the origin, θ is the polar angle, and ϕ is the azimuthal angle about the axis of symmetry z (Fig. 1), $\{v_r, v_\theta, v_\phi\}$ are velocity components, Ψ is the Stokes stream function, and the prime denotes (here and in the paper remainder) differentiation with respect to $x=\cos\theta$.

Substitution of (1) in the Navier–Stokes equations in spherical coordinates (e.g., Ref. [17]), exclusion of pressure, and simple calculations yield the system of ordinary differential equations [8],

$$(1-x^2)\psi' + 2x\psi - \tfrac{1}{2}\psi^2 = F, \tag{2a}$$

$$(1-x^2)F''' = 2\Gamma_b\Gamma_b', \tag{2b}$$

$$(1-x^2)\Gamma_b'' = \psi\Gamma_b', \tag{2c}$$

where F is an auxiliary function defined by Eq. (2b). The boundary conditions on the symmetry axis, $x=1$ (i.e., $\theta=0$), are

$$\psi = 0, \ \Gamma_b = \mathrm{Re}_s, \quad F' = 2A. \tag{2d}$$

The first condition of (2d) indicates that the axis is free from a source of fluid, the second condition specifies a given circulation, so that swirl velocity, v_ϕ, has a pole singularity for $\mathrm{Re}_s \neq 0$ according to (1), and the third condition specifies a given axial force which corresponds to a logarithmic singularity of the radial velocity, v_r [5]. These two singularities—the line sources of angular and axial momenta located on the symmetry axis—model an entrainment flow driven by a swirling near-axis jet whose thickness is neglected. We show below that this flow has multiple states at the same values of Re_s and A.

It follows from (2a) and (2d) that

$$F(1) = 0. \tag{2e}$$

We generalize the Serrin problem [5] to a flow inside a cone, i.e., between the axis, $x=1$, and a conical wall, $x=x_c$, where the no-slip condition yields that

$$\psi = \Gamma_b = F = 0 \quad \text{at } x = x_c. \tag{2f}$$

In the particular case, $x_c=0$ (i.e., $\theta=90°$), the conical surface, $x=x_c$, reduces to the normal-to-axis plane and the problem reduces to the Serrin one. We address here the cone geometry because (a) some vortex devices, e.g., hydrocyclones and Ranque tubes, have conical walls, (b) hysteretic transitions occur, and (c) analytical solutions can be obtained in this more generic case as well.

Now we explore asymptotic solutions as $\mathrm{Re}_s \to \infty$. For $\mathrm{Re}_s \gg 1$, the linear term in the left-hand side of (2c) becomes negligible, i.e., (2c) reduces to $\psi\Gamma_b' = 0$, and therefore Γ_b' tends to 0, except at points where $\psi = 0$, i.e., the limiting $\Gamma_b(x)$ is a step function. Owing to the different boundary conditions of $\Gamma_b(x_c)=0$ and $\Gamma_b(1)=\mathrm{Re}_s$, $\Gamma_b(x)$ must jump at some $x=x_s$. Consider, first, the case where the jump occurs at an inner point of the interval, i.e., $x_c < x_s < 1$. Since Γ_b' is unbounded at $x=x_s$, $\psi(x_s)$ must be zero, and, therefore, the conical surface, $x=x_s$, separates different flow cells (see inset B in Fig. 2). Inside each cell, the circulation is uniform and equal to the corresponding boundary values,

$$\Gamma_b(x) = 0 \quad \text{for } x_c \leqslant x < x_s \ \text{(near-wall region 1)}, \tag{3a}$$

$$\Gamma_b(x) = \mathrm{Re}_s \quad \text{for } x_s < x \leqslant 1 \ \text{(near-axis region 2)}. \tag{3b}$$

Next, $\Gamma_b' = 0$ reduces (2b) to $F''' = 0$ and therefore, $F(x)$ is a quadratic polynomial (different in regions 1 and 2). Satisfying conditions (2d)–(2 f) yields

$$F_1(x) = -b(x-x_c)^2, \tag{4a}$$

$$F_2(x) = -\frac{1}{2}\mathrm{Re}_s^2[(1-P)(1-x) - c(1-x)^2], \tag{4b}$$

where subscripts 1 and 2 denote F in regions 1 and 2, respectively, and $P = 1 + 4A/\mathrm{Re}_s^2$. To determine b, c, and P as functions of x_s and Re_s, consider matching conditions at the separating surface $x=x_s$. At this surface, $F(x)$ and $F'(x)$ are continuous while $F''(x)$ undergoes a jump whose value follows from integration of (2b) across $x=x_s$,

$$F_1(x_s) = F_2(x_s), \quad F_1'(x_s) = F_2'(x_s),$$

$$F_2''(x_s) - F_1''(x_s) = \mathrm{Re}_s^2/(1-x_s^2). \tag{5}$$

From (4) and (5) we obtain

$$b = \frac{1}{2}\mathrm{Re}_s^2(1-x_s)(1+x_s)^{-1}(1-x_c)^{-2} > 0, \tag{6a}$$

$$c = (x_s - x_c)(2 - x_s - x_c)(1-x_s^2)^{-1}(1-x_c)^{-2} > 0, \tag{6b}$$

$$P = (1-x_s)(1+x_s)^{-1}(1+x_c)(1-x_c)^{-1}. \tag{6c}$$

It follows also that $F(x) \leqslant 0$ in the entire interval, $x_c \leqslant x \leqslant 1$.

For $\mathrm{Re}_s \gg 1$, the linear terms on the left-hand side of (2a) become negligible, and (2a) reduces to $\psi^2 = -2F$ resulting in

$$\psi_1(x) = [-2F_1(x)]^{1/2} = (2b)^{1/2}(x-x_c) \quad \text{and}$$

$$\psi_2(x) = -[-2F_2(x)]^{1/2}. \tag{7}$$

The different signs of ψ_1 and ψ_2 in (7) are due to different flow directions in the cells (see inset B in Fig. 2). As a result,

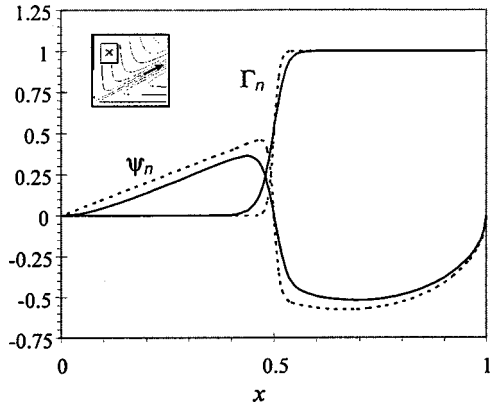

FIG. 3. Comparison of the numeric (solid curve, $\mathrm{Re}_s=200$) and analytical (broken curve, $\mathrm{Re}_s\to\infty$) solutions for a two-cell Serrin flow. Γ_n and ψ_n are normalized circulation and stream function, $x=\cos\theta$, and the inset shows the flow pattern.

there is a jump in $\psi(x)$ from $\psi_1(x_s)=\psi_s$ to $\psi_2(x_s)=-\psi_s$ as increasing x passes x_s, where $\psi_s=(2b)^{1/2}(x_s-x_c)$.

The jumps in circulation and stream function indicate that there is a viscous boundary layer near the separating surface, $x=x_s$, where as x increases, $\psi(x)$ decreases from ψ_s to $-\psi_s$ and $\Gamma_b(x)$ increases from 0 to Re_s according to (3).

In this boundary layer, (2a) and (2c) reduce to

$$(1-x_s^2)\psi'+2x_s\psi-\frac{1}{2}\psi^2=-\psi_s^2 \quad \text{and} \quad (1-x_s^2)\Gamma_b''=\psi\Gamma_b'.$$

Introducing the "inner" variables, $V=-\psi/\psi_s$ and $\xi=\psi_s(x-x_s)/(1-x_s^2)$, and allowing $\psi_s\to\infty$, we get $dV/d\xi=1-V^2$, $V=\tanh\xi$, and

$$\psi_{\mathrm{in}}=-\psi_s\tanh\xi, \quad \Gamma_{\mathrm{in}}=\frac{1}{2}\mathrm{Re}_s(1+\tanh\xi). \tag{8}$$

where subscript "in" denotes the *inner* solutions (i.e., within the boundary layer). These solutions describe a jet directed radially outward along the separating surface (inset B in Fig. 2).

The solution, $\Gamma=\frac{1}{2}\mathrm{Re}_s(1+\tanh\xi)$, can serve also as a uniform approximation for circulation in the entire flow region. To get a uniform approximation for stream function, we should combine the inviscid, (7), and boundary-layer, (8), solutions to construct a composite solution [18]:

$$\psi_c(x)=-\psi_1(x)\tanh\xi \quad \text{for } x_c<x\leqslant x_s$$

$$\text{and } \psi_c(x)=\psi_2(x)\tanh\xi \quad \text{for } x_s\leqslant x<1. \tag{9}$$

Here subscript c denotes the *composite* solution.

To determine the parameter range where this solution exists we address (6c) which provides the relation between P and x_s. As x_s increases from x_c to 1, P decreases from 1 to 0. Therefore, the two-cell solution exists in the range $0<P<1$ as $\mathrm{Re}_s\to\infty$ (see Fig. 2 where large Re_s correspond to a vicinity of the abscissa).

Figure 3 shows the numerical (solid curves) and composite asymptotic (dashed curves) solutions at $x_c=0$, $x_s=0.5$ ($P=1/3$), and $\mathrm{Re}_s=200$; $\psi_n=\psi(2b)^{1/2}$ and $\Gamma_n=\Gamma/\mathrm{Re}_s$. The inset shows streamlines and flow direction (arrow). To obtain the numerical solution, we integrate (2) from $x=x_s$ in the both directions (to $x=1$ and to $x=x_c$) starting with $\psi=0$ and tentative values of Γ, Γ', F, F', and F'' at $x=x_s$. Then we adjust these tentative values to satisfy (2f) and the first and second conditions (2d). The third condition (2d) specifies A (and P), as a function of x_s. The numerical and analytical solutions are close but do not coincide at this value of Re_s. In particular, the analytical solution does not describe the boundary layer near $x=x_c$, because it does not satisfy the condition $\psi'(x_c)=0$ that follows from no-slip.

Now we show that the one-cell solution, corresponding to a descending flow (inset A in Fig. 2), exists at the same parameter values as those where the two-cell flow occurs. For the descending flow, Serrin [5] proved the existence theorem at $x_c=0$. Here we construct an analytical solution for any x_c and $\mathrm{Re}_s\gg1$. For this one-cell case, region 2 defined in (3b) occupies the entire flow domain. Therefore, the inviscid solution for circulation is

$$\Gamma_{bo}(x)=\mathrm{Re}_s \quad \text{for } x_c<x\leqslant 1. \tag{10a}$$

The condition (2f), $F(x_c)=0$, and (4b) yield $c=(1-P)(1-x_c)^{-1}$ resulting in

$$F_o=-\frac{1}{2}\mathrm{Re}_s^2(1-P)(1-x)(x-x_c)(1-x_c)^{-1}, \tag{10b}$$

$$\psi_o(x)=-[-2F_o(x)]^{1/2}=-\frac{1}{2}\mathrm{Re}_s[(1-P)(1-x)(x-x_c)(1-x_c)^{-1}]^{1/2}. \tag{10c}$$

Subscript o indicates that solutions (10) are valid *outside* a near-wall boundary layer.

Figure 4 shows the outer solution (10) (dashed curves) and numerical results (solid curves) at $x_c=0$, $x_s=0$, $P=0.708$, and $\mathrm{Re}_s=100$ [$\psi_n=\psi\,\mathrm{Re}_s^{-1}(1-P)^{-1/2}$ and $\Gamma_n=\Gamma/\mathrm{Re}_s$]. The inset shows streamlines and the flow direction (arrow). As demonstrated, sufficiently away from the wall, the analytical and numerical solutions are close to each other while the two solutions are well apart near the wall. In the latter case, a viscous layer develops because $\psi_o'(x)$ is unbounded and $\Gamma_{bo}(x)\neq0$ at $x=x_c$.

To find the boundary-layer solution, we introduce the inner variables,

$$\eta=B(x-x_c), \quad W=-\psi/[B(1-x_c^2)],$$

$$\gamma=\Gamma/\mathrm{Re}_s, \quad \text{and } \Phi=-B^2(1-x_c^2)F\,\mathrm{Re}_s^{-2},$$

where $B=\mathrm{Re}_s^{1/2}(1-x_c^2)^{-3/4}$. Applying this transformation in (2a)–(2c), and allowing $\mathrm{Re}_s\to\infty$, we obtain the system

$$\frac{dW}{d\eta}=\Phi-\frac{1}{2}W^2, \quad \frac{d^2W}{d\eta^2}=-W\frac{d\gamma}{d\eta}, \quad \frac{d^2\Phi}{d\eta^2}=1-\gamma^2. \tag{11}$$

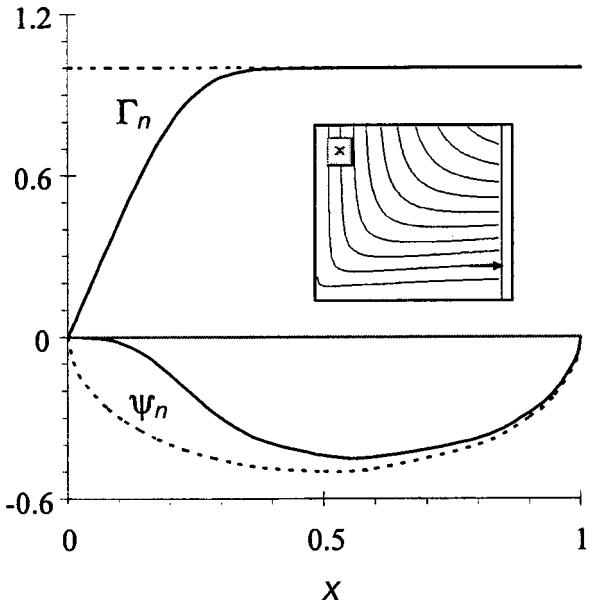

FIG. 4. Comparison of the numeric (solid curve, $\mathrm{Re}_s=100$) and analytical (broken curve, $\mathrm{Re}_s\to\infty$) solutions for a one-cell descending Serrin flow (see Fig. 3 for other notations).

The no-slip boundary conditions are

$$W(0)=\Phi(0)=\gamma(0)=0. \tag{12}$$

Matching with the outer solution (10) yields two more conditions,

$$\gamma\to 1 \quad \text{and} \quad \frac{d\Phi}{d\eta}\to\frac{1}{2}(1-P)\mathrm{Re}_s^{1/2}(1-x_c)^{1/4} \quad \text{as} \quad \eta\to\infty. \tag{13}$$

Alternatively, we can consider $d\Phi/d\eta(\infty)$ as a free parameter (>0) and find that

$$P=1-2\,\mathrm{Re}_s^{-1/2}(1-x_c)^{-1/4}\frac{d\Phi}{d\eta}(\infty). \tag{14}$$

This boundary-layer solution describes a near-wall swirling jet directed away from the symmetry axis (inset A in Fig. 2) and also a two-cell flow (inset B in Fig. 2) when the second cell and the separating surfaces are inside the near-wall boundary layer.

We have solved problem (11)–(13) numerically using the following algorithm. Integration of (11) starts at $\eta=0$ with conditions (12) and tentative values of $d\Phi/d\eta(0)$ and $d\gamma/d\eta(0)$. We run the integration up to $\eta=\eta_f$. Then we adjust $d\Phi/d\eta(0)$ and $d\gamma/d\eta(0)$ by a shooting procedure to satisfy conditions (13) at $\eta=\eta_f$. Next we increase η_f until values of $d\Phi/d\eta(0)$ and $d\gamma/d\eta(0)$ become well established (to this end, $\eta_f=10$ appears to be sufficient).

Figure 5 shows the dependence of $d\Phi/d\eta(0)=d^2W/d\eta^2(0)$, which is proportional to the radial shear stress at the wall, on $d\Phi/d\eta(\eta_f)$ [which is very close to $d\Phi/d\eta(\infty)$]. As demonstrated, two flow states occur at the same values of $d\Phi/d\eta(\infty)$, i.e., at the same values of P (when Re and x_c are fixed), as follows from (14). The two solution branches merge (and then disappear) as $d\Phi/d\eta(\eta_f)$ decreases (and passes the fold point F). Point S separates one-cell ($1c$) and two-cell ($2c$) flows (see insets A and B in Fig. 2).

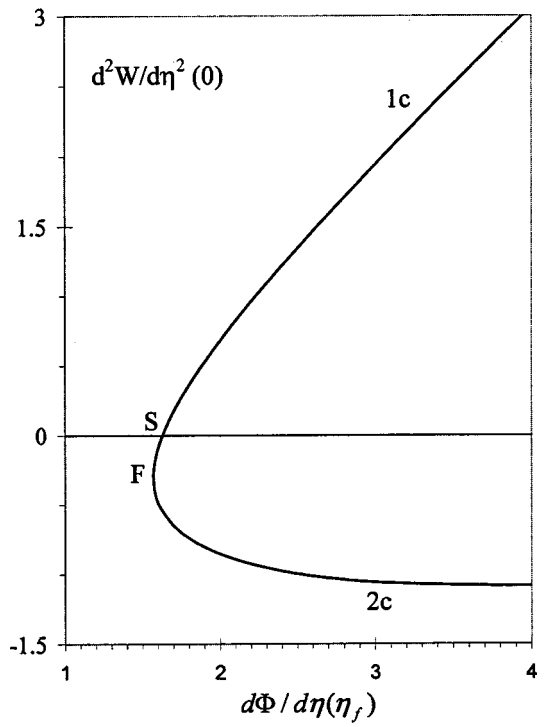

FIG. 5. Two solution branches for the near-wall boundary layer in the Serrin problem. The branches merge and terminate at the fold point F. The flow is one-cellular ($1c$) and two-cellular ($2c$) above and below point S, where the flow separation from the wall occurs.

Figure 6 shows profiles of the radial ($dW/d\eta$) and swirl (γ) velocities in the near-wall boundary layer at $d\Phi/d\eta(\infty)=3$ for the one-cell (a) and two-cell (c) flows. Figure 6(b) shows the profiles at point S in Fig. 5 where the flow separation from the wall occurs. These profiles describe in more detail the near-wall jet sketched by inset A in Fig. 2.

We see that for any fixed $\mathrm{Re}_s\gg 1$ and $P<1$ [this limitation follows from (10c)], two branches of solutions exist. This

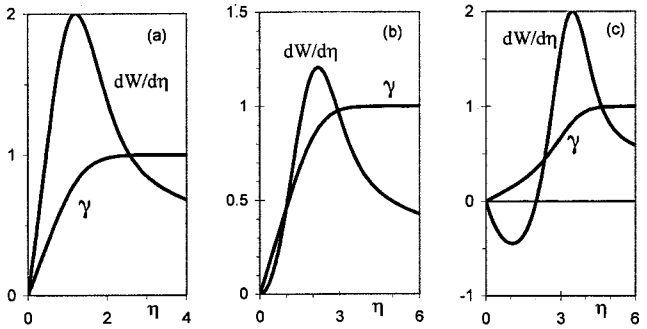

FIG. 6. Profiles of the radial ($dW/d\eta$) and swirl (γ) velocities in the near-wall boundary layer for the one-cell (a), separation (b), and two-cell (c) flows (for points $1c$, S and $2c$ in Fig. 5, respectively). The variable η is the scaled distance from the wall.

result explains why Serrin [5] failed to prove the uniqueness theorem, and, in addition, indicates that two flow states can occur at the same values of control parameters for any conical (not only planar) wall.

Thus, the results of Sec. II A reveal that hysteresis is a typical feature of the Serrin [5] model describing near-wall swirling flows. Hysteresis is a typical feature for the Long model [19] of free swirling jets as well [11]. Unfortunately, both these models have serious limitations.

The Serrin model involves singularities on the axis and, therefore, describes practical flows away from the axis only. In contrast, the Long model well describes the near-axis flow but does not satisfy the no-slip condition at a wall. A reason for these limitations is the fact that a regular conical solution, satisfying both the no-sip condition on a wall and the regularity condition on the axis, is identically zero (the rest state).

Somewhere a source of fluid motion must be located. This source is on the axis in the Serrin model and on the conical flow boundary in the Long model. To better model practical flows, where both the near-axis and near-wall regions are important, e.g., tornadoes and vortex precession, it is reasonable to locate a source of motion (i.e., a singularity) somewhere in between the axis and the wall. We develop such a model and explore its features in the next section.

B. Hysteresis in a weak-singularity model of the near-wall vortex

A swirling jet has at least two sources of motion: one for the meridional flow and another for the swirl. Here we model these sources by weak singularities located away from both the axis and the wall. We place these singularities on a conical surface, $x=x_j$, separating regions of the upward and downward flows where the vertical velocity $v_z=v_r\cos\theta - v_\theta\sin\theta$ vanishes, i.e., $v_z(x_j)=0$. A motivation for such a choice is that in practical wall-normal vortices (e.g., in tornadoes), circulation is transported by a horizontal wind from a remote region toward the vortex axis. Therefore, the surface where the velocity is horizontal seems to be an appropriate location for motion sources.

At this surface, $x=x_j$, we prescribe jumps in F'' and Γ_b'. The F'' jump serves as a source of the meridional motion (when the flow is even swirl free as well) and the Γ_b' jump serves as a source of swirl. Indeed, we will see that circulation, Γ_b, achieves its maximum at $x=x_j$. Accordingly, to characterize the strength of rotation, we define the swirl Reynolds number as a ratio of the maximum circulation to viscosity, $\mathrm{Re}_s=\Gamma_b(x_j)$. To characterize the strength of the meridional flow, we use the Long parameter M, which is a ratio of the axial flow force to the maximum circulation squared, $M=2\pi J_0/\mathrm{Re}_s^2$, where

$$J_0=\int_0^1 (x\{(2-\psi')\psi'-[(2x-\psi)\psi-xF'](1-x^2)^{-1}\} - F')dx \tag{15}$$

(for more details see Ref. [11]). Since, for conical flows, the tangential stresses and pressure (scaled by $\rho\nu^2r^{-2}$) are

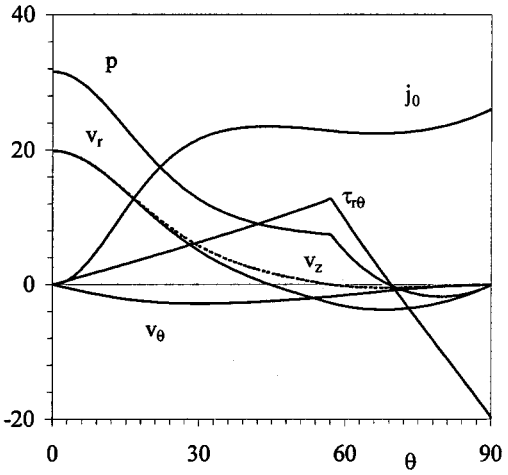

FIG. 7. Dependence of the velocity components, shear stress, pressure, and the flow force density on the polar angle θ for a swirl-free jet induced by a weak singularity (jump in the $\tau_{r\theta}$ slope).

$$\tau_{\phi\theta}=\Gamma_b'+(2x-\psi)\Gamma_b(1-x^2)^{-1},\quad \tau_{r\theta}=-F'(1-x^2)^{-1/2},$$

$$\text{and}\quad p=(2x\psi-xF'-\psi^2)(1-x^2)^{-1},$$

$\tau_{\phi\theta}$ can have a jump while $\tau_{r\theta}$ and p are continuous at $x=x_j$.

The numerical algorithm to solve this problem is briefed here. Integration of (2a)–(2c) starts at $x=1$ with $\psi(1)=\Gamma_b(1)=F(1)=F'(1)=0$ and tentative values of $\Gamma_b'(1)$, $F''(1)$, and $\psi'(1)$. [The latter value cannot be determined from (2a) due to the 0/0 indeterminacy.] First, integration runs up to $x=x_j$ where we introduce the jumps, $\delta\Gamma_b'$ and $\delta F''$, in Γ_b' and F''. Then the integration continues up to the wall, $x=x_c$. Next we adjust $F''(1)$, $\psi'(1)$, $\delta\Gamma_b'$, and $\delta F''$ to satisfy $v_z(x_j)=0$ and the no-slip conditions $\psi(x_c)=\Gamma_b(x_c)=F(x_c)=0$. Values of $\Gamma_b'(1)$ and x_j remain free and implicitly specify Re_s and M; the later two serve as control parameters. The results described below are for the planar wall, $x_c=0$.

Figure 7 shows the results of calculation for a swirl-free normal-to-wall jet induced by a weak singularity at $x_j=0.537$ (or $\theta_j=57.5°$). All velocity and stress components as well as the axial-flow-force density (j_0) are continuous while slopes of pressure p and $\tau_{r\theta}$ undergo jumps at $\theta=\theta_j$. The flow is close to the Schlihting [20] round jet near the axis though the axial Reynolds number, $\mathrm{Re}_a=rv_a/\nu$, is moderate ($\mathrm{Re}_a=20$); v_a is the velocity on the axis.

This swirl-free jet depends on the flow force, J_0, in a simple way without folds and hysteresis. Multiple flow states appears as the swirl Reynolds number, Re_s, exceeds its threshold. Figure 8 shows a map of the flow state on the plane of control parameters M and Re_s. For small Re_s, there is a single flow state at each value of M. This is clearly illustrated by the $\mathrm{Re}_s=16$ curve in Fig. 9. This figure plots the maximum swirl velocity $v_{\phi\,\max}$ versus the flow force (M) at $\mathrm{Re}_s=16$, 23, and 30 (also indicated in Fig. 8). As Re_s increases, the slope at the inflection point becomes vertical (e.g., the star symbol on the $\mathrm{Re}_s=23$ curve in Fig. 9, which

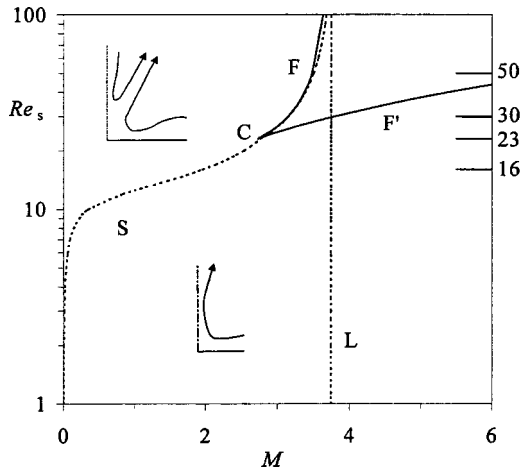

FIG. 8. Map of the flow patterns on the plane, {flow force M, swirl Reynolds number Re_s}, for the weak-singularity model. Curve S separate one-cell (lower inset) and two-cell (upper inset) flows. There are three flow states in the region between folds F and F' which merge and terminate at cusp point C. Line L shows the Long [19] asymptote for fold F as $\mathrm{Re}_s \to \infty$.

correspond to cusp C in Fig. 8), and then three solution branches develops (e.g., I, II, and III of the $\mathrm{Re}_s=30$ curve in Fig. 9). As M increases (or decreases), jump transitions (arrows) between two stable flow states (I and III) must occur at the fold point F' (or F) along the $\mathrm{Re}_s=30$ curve. Intermediate branch II represents the unstable state.

Curve S in Fig. 8 separates regions of one-cell (lower inset) and two-cell (upper inset) flows. Folds F and F' (see the $\mathrm{Re}_s=30$ curve in Fig. 9) merging at cusp C ($M=2.73$, $\mathrm{Re}_s=23$) bound the region where three flow states exist at any M and Re_s (e.g., the $\mathrm{Re}_s=30$ curve in Fig. 9). Outside the region, the steady state is unique. The vertical line L at $M=3.74$ is Long's asymptote to F as $\mathrm{Re}_s \to \infty$. As Re_s increases, the three-flow-state region expands for a large range of M.

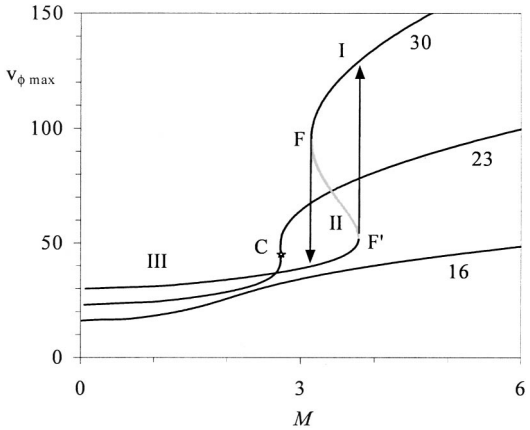

FIG. 9. Development of cusp C and folds F and F' as Re_s (shown near the curves) increases. The symbol $v_{\phi\,\max}$ is the maximum swirl velocity as θ varies at a fixed r. I, II, III mark different solution branches and the arrows sketch hysteretic transitions among flow states.

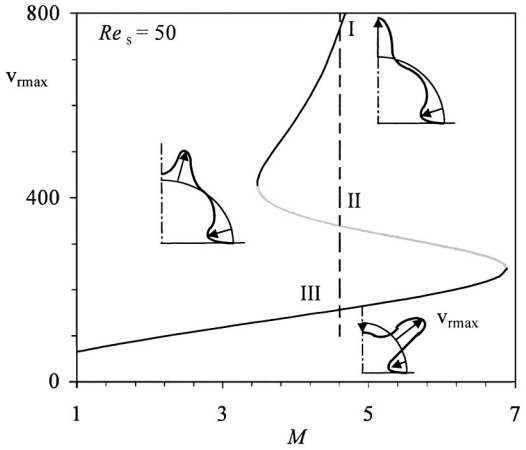

FIG. 10. Multiple flow states I, II, and III (see also insets) at $\mathrm{Re}_s=50$. The symbol $v_{r\,\max}$ denotes the maximum radial velocity as θ varies at a fixed r.

Figure 10 shows the three solution branches at $\mathrm{Re}_s=50$. In the consolidated jet, the outflow focuses near the axis and the velocity on the axis is also the maximum radial velocity $v_{r\,\max}$ as θ varies at a fixed r [see Fig. 11(a) and the upper inset for point I in Fig. 10]. All velocity and stress components reach their maximum values also near the axis [Fig. 11(b)]. Since $\mathrm{Re}_s\,(=50)$ is rather large, this flow demonstrates some asymptotic features. In particular, there is a wide interval of the polar angle θ, where circulation Γ_b is nearly uniform and close to its maximum value $\mathrm{Re}_s=50$ [Fig. 11(c)]. The flow coincides with the consolidated Long jet in the near-axis region $0 \leqslant \theta < \theta_j$ but differs in the near-wall region $\theta_j < \theta \leqslant 90°$.

Solutions at point II and III in Fig. 10 represent annular jets where the velocity on the axis differs from $v_{r\,\max}$. The flow is one-cellular for solution II (the middle inset in Fig. 10) while the axial velocity is negative and the flow is two-cellular for solution III (Fig. 12 and the lower inset in Fig. 10). The solution III, Fig. 12, is close to the two-cell annular flow calculated in Ref. [11] inside the region $0 \leqslant \theta < \theta_j$, but these two flows differ in the vicinity of the wall. The dashed branch in Fig. 10 depicts unstable solutions, e.g., at point II.

Thus, three flow states can exist at the same values of control parameters. This feature is common for the Long, Serrin, and the weak-singularity (considered in this section) models. We conclude that multiple flow states and hysteretic transitions among them are typical of near-wall swirling flows independent of where the motion sources are located: on the axis, on the wall or in between. The hysteretic transitions occur via time-monotonic disturbances as shown in Refs. [12] and [21,22]. In contrast, the axisymmetry breaking and precession development are due to time-oscillatory instability, as discussed below.

III. THE STABILITY PROBLEM

The stability equations for conical flows are derived in Ref. [13]. Use of the new dependent and independent variables (as wells as the normal-mode technique) reduces the linear stability problem to a system of ordinary differential equations (ODE). The new dependent variables are

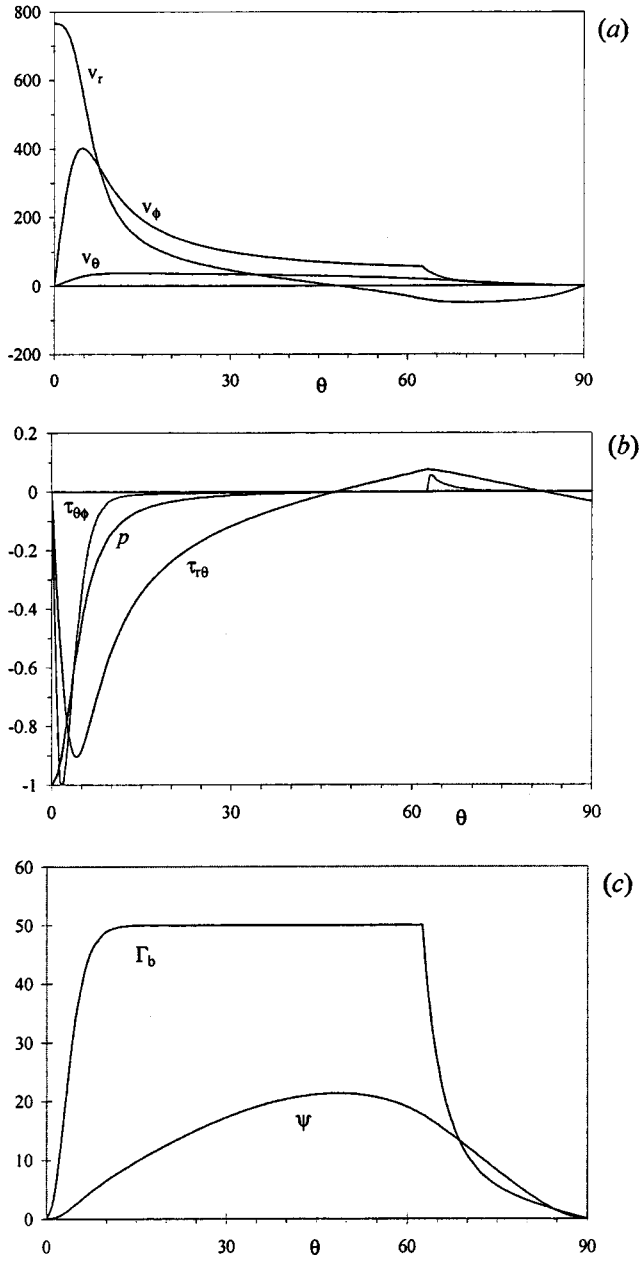

FIG. 11. Dependence of (a) velocity, (b) stress, and (c) circulation Γ_b and stream function ψ on polar angle θ for solution I in Fig. 10.

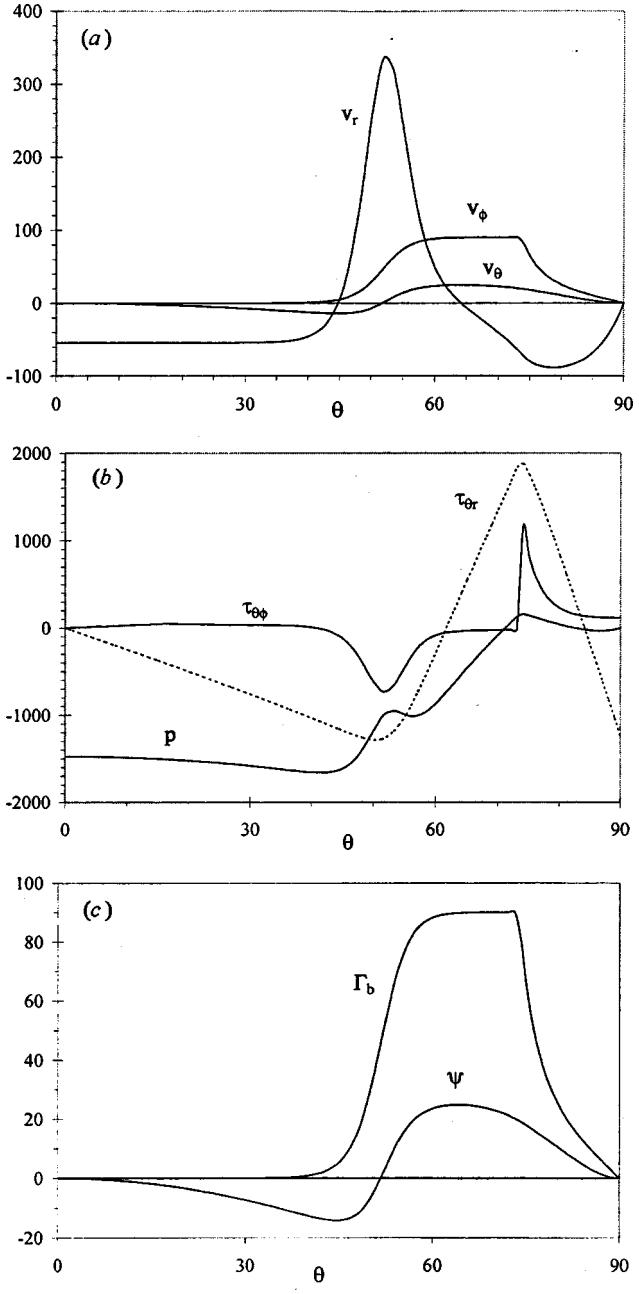

FIG. 12. The same as in Fig. 11 but for solution III in Fig. 10.

$$u(x,\phi,\xi,\tau)=v_r r/\nu, \quad v(x,\phi,\xi,\tau)=v_\theta r\sin\theta/\nu,$$

$$\Gamma(x,\phi,\xi,\tau)=v_\phi r\sin\theta/\nu,$$

$$p(x,\phi,\xi,\tau)=(\underline{p}-\underline{p}_\infty)r^2/(\rho\nu^2),$$

where dimensionless variables u, v, Γ, and p correspond to the velocity components $\{v_r, v_\theta, v_\phi\}$ and the pressure $\underline{p}$, respectively; $\underline{p}_\infty$ represents a limiting pressure as $r\to\infty$, ρ is the (constant) density, and ν is the kinematic viscosity. The new independent variables are

$$\xi=\ln(r/r_0), \quad x=\cos\theta, \quad \text{and} \quad \tau=\nu t/r^2,$$

where a length scale r_0 makes the argument of the logarithm dimensionless. The normal mode representation for disturbances is

$$u=u_b(x)+u_d(x)E+\text{c.c.}, \quad v=v_b(x)+v_d(x)E+\text{c.c.},$$

$$p=p_b(x)+p_d(x)E+\text{c.c.}, \quad \Gamma=\Gamma_b(x)+i\Gamma_d(x)E+\text{c.c.},$$

where $E=\exp(a\xi+im\phi-i\omega\tau)$, c.c. denotes the complex conjugate of the preceding complex term, complex $\alpha=\alpha_r+i\alpha_i$ where α_r is the growth of the spatial mode with the radial distance and α_i is a radial wave number, m is an (integral)

azimuthal wave number, ω is the dimensionless frequency, and the subscripts b and d indicate base flow and disturbance, respectively.

The real part α_r of exponent α characterizes the spatial stability, as r increases, if $\alpha_r<0$, the disturbance decays faster than the base flow; if $\alpha_r=0$, the disturbance amplitude and the base flow have the same r dependence (their velocities decay as r^{-1}); and if $\alpha_r>0$, the ratio of disturbance to the base flow amplitude increases with r. Hence, $\alpha_r<0$, $\alpha_r=0$, and $\alpha_r>0$ correspond to spatial stability, neutral stability, and instability of the base flow, respectively.

We consider a flow above the plane $x=0$, with the jet source (vortex and radial velocity singularities) located on the axis of symmetry, z (Fig. 1). Therefore, the flow region is $0\leqslant x<1$. The axis of symmetry is a source of motion where the vortex singularity (i.e., nonzero circulation) and the axial force are given for the base flow. This yields that $u_d(1)=0$. The other boundary conditions, $v_d(1)=\Gamma_d(1)=0$ and $v_d(0)=\Gamma_d(0)=u_d(0)=0$, are the same as in Ref. [13].

To find a nontrivial (eigen)solution for the normal modes, we should seek complex eigenvalues of either α for a given real ω (spatial stability) or ω for $\alpha_r=0$ (temporal stability). This paper focuses on neutral disturbances, for which the results of the spatial and temporal stability approaches are identical (since $\alpha_r=0$ and ω is real). However, to find neutral characteristics of the Serrin vortex, we use the spatial stability approach. The reason is that all eigenvalues of α are known for $\mathrm{Re}_s=A=\omega=0$ and any m [20]. Eventually, by increasing Re_s and A (which characterize the strength of the base flow), as well as frequency ω, we find α by the Newton shooting procedure using the α value found at previous parameters for an initial guess. Applying this algorithm for a few spectral branches (that have the largest α_r at $\mathrm{Re}_s=A=0$) we find what disturbance mode is the most dangerous, i.e., have the smallest critical values of Re_s and A. The numeric technique of the stability studies is similar to that described in Ref. [13].

IV. INSTABILITY OF THE SERRIN VORTEX

Figure 13 shows the results for the Serrin vortex on the control parameter plane (axial-force strength A, swirl Reynolds number Re_s). Curve C corresponds to the collapse of the Serrin jet, the regular solution exists only below this curve for $A>0$. This solution describes a one-cell ascending flow (right inset). For $A<0$, the flow map is more complicated. There are descending one-cell flows in the region below curve S (lower inset) and two-cell flows above curve S (upper inset). Two flow states occur at the same A and Re_s in the region bounded by curves C and F. The corresponding solutions merge and disappear as Re_s increases and passes the fold curve F. One of these solutions terminates as decreasing Re_s passes the collapse curve C, while the other exists for any $|\mathrm{Re}_s|<\mathrm{Re}_f$ where $\mathrm{Re}_f(A)$ is a value of Re_s on curve F.

We have found that as Re_s increases, the $m=1$ helical mode first becomes growing. Curve I ("Instability") shows the critical values of Re_s as a function of A. For $A\geqslant 0$, the instability occurs for smaller Re_s than $\mathrm{Re}_s=\mathrm{Re}_{\mathrm{col}}$ corresponding to the collapse (accordingly, curve I is below curve C in Fig. 13). At $A=0$, for instance, the critical Reynolds number of the $m=1$ instability is $\mathrm{Re}_s=5.05$ while the collapse value is $\mathrm{Re}_s=5.53$.

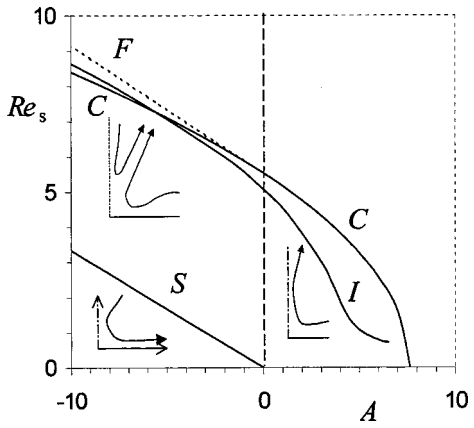

FIG. 13. Flow and stability map on the plane, {swirl Reynolds number Re_s, axial force A}. Vertical (dashed) and S lines separate regions of different flow patterns (see insets). Curves C and F show where collapse and fold occur. The flow is stable (unstable) below (above) curve I.

For $A<0$, the instability can occur at either smaller or larger Re_s than $\mathrm{Re}_{\mathrm{col}}$, depending on the magnitude of A. The critical Re_s can exceed $\mathrm{Re}_{\mathrm{col}}$ because the corresponding flow belongs to the solution sheet that spreads from the abscissa, $\mathrm{Re}_s=0$, up to the fold curve F in Fig. 13. A part of this sheet (which is located above curve I up to curve F) and the other sheet (which is located between curves F and C) correspond to unstable flows.

Consider this instability in more detail for a specific value of A. To this end, we choose $A=0$ (i.e., no axial force acting), where the axial Reynolds number, $\mathrm{Re}_a=rv_a/\nu$, where v_a is the velocity on the axis, is bounded for a regular solution. The critical parameters at $A=0$ are $\mathrm{Re}_a=36.4$, $\alpha_i=2.66$, $\omega=-3$. Figure 14 shows (a) frequency $\underline{\omega}=\omega/\mathrm{Re}_a$, (b) radial wave number α_i, and (c) phase velocity $C=\underline{\omega}/\alpha_i$ for neutral disturbances (real ω and $\alpha_r=0$) as Re_a varies. C is the disturbance wave speed normalized by the base-flow velocity on the axis.

Positive ω indicates that the helical disturbances rotate around the axis in the same sense as the base swirling flow, and negative ω corresponds to counter-rotating disturbances. Figure 14(a) shows that the critical disturbance (occurring at the smallest Re_a) is counter-rotational (because $\omega<0$). While frequency changes its sign along the neutral curve, the wave number remains positive [Fig. 14(b)]. The phase speed of neutral disturbances changes its sign [Fig. 14(c)] together with ω. Positive C corresponds to disturbance waves propagating downstream in the base flow and negative C corresponds to waves propagating upstream.

Since the disturbance energy propagates not with the phase but group speed (speed of a wave group) we have also calculated the group speed, $C_g=d\underline{\omega}/d\alpha_i$, at each point of the neutral curve. Figure 15 shows both the group (solid curve) and phase (dotted curve) for comparison. While moving along the neutral curve from the upper to lower branch,

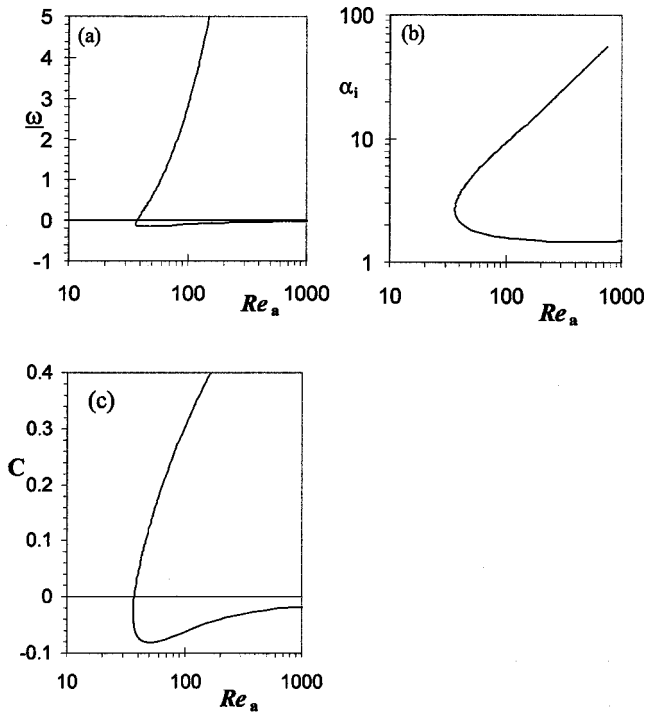

FIG. 14. Axial Reynolds number (Re_a) dependence of (a) frequency, (b) radial wave number, and (c) phase velocity of neutral disturbances in the case of no axial force ($A=0$).

first the phase speed becomes negative (close to the critical point on the upper branch), and then the group speed becomes negative (at $\mathrm{Re}_a=250$ and $\alpha_i=1.48$ on the lower branch). Therefore, the instability is convective for Re_a close to the critical value and becomes absolute for large Re_a (>250).

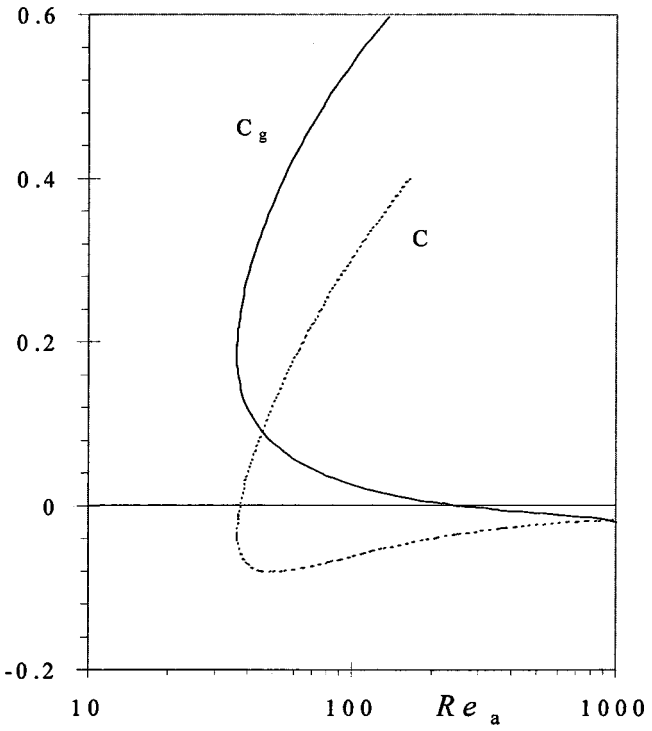

FIG. 15. Group (C_g, solid curve) and phase (C, dotted curve) of neutral disturbances ($A=0$).

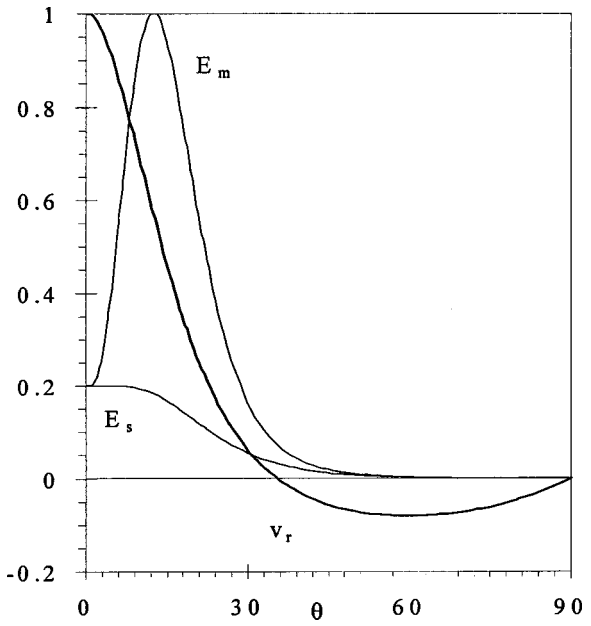

FIG. 16. Radial velocity of the base flow (v_r) and disturbance meridional (E_m) and swirl (E_s) kinetic energy dependence on polar angle θ for the critical Reynolds number at $A=0$. The fact that disturbance energy reaches its maximal near the inflection point of the base flow indicates the shear-layer character of the instability.

Figure 16 shows the radial velocity profile for the base flow, v_r, and the disturbance kinetic energy, separately for the meridional, $E_m=|u_d|^2+|v_d|^2/(1-x^2)$, and swirl, $E_s=|\Gamma_d|^2/(1-x^2)$, components at the critical value of $\mathrm{Re}_a=36.4$. Since E_m is significantly larger than E_s, the instability affects more the meridional flow (v_r and v_θ) rather than the swirl (v_ϕ). The fact that E_m reaches its maximum near the inflection point of $v_r(\theta)$ indicates the shear-layer mechanism of instability.

Thus, the critical disturbance is counter-rotating ($\omega<0$) and develops due to shear-layer instability. Such an instability being single-helical ($m=-1$) shifts the jet center away from and rotates the jet around the axis of symmetry of the base flow, i.e., induces the development of jet precession. To describe the finite-amplitude precession, the nonlinear stability and bifurcation of the secondary flow state established must be studied. This is beyond the scope of this paper and a subject for further study.

V. CONCLUSIONS

To understand the mechanisms of multiple flow states and precession, two intriguing and practically important phenomena observed in vortices normal to a wall, we have considered conically similar models of the base flow and have explored the flow stability.

New analytical solutions of the Navier–Stokes equations obtained herein explain the multiple flow states in the Serrin model of a near-wall vortex. In addition, we have developed a new model where no singularity occurs on the vortex axis.

This model well describes both the near-axis (in contrast to the Serrin model [5]) and near-wall (in contrast to the Long model [19]) flow regions. A weak singularity on a conical surface located away from both the axis and wall models forces driving the flow. This singularity corresponds to jumps in the swirl shear stress and in the slopes of the meridional shear stress and pressure.

Our numerical results for this model show that folds and hysteresis develop as the swirl Reynolds number exceeds a threshold. These results, together with those for the Serrin (this paper) and Long (Shtern and Hussain [11]) models, suggest that multiple flow states are typical of the near-wall swirling flows, regardless of where the driving forces are applied.

To explore the precession mechanism, we have extended a new stability approach for (strongly nonparallel) conical flows [13] to the Serin model where singularities are located on the axis. Numerical solutions of this stability problem reveal that, as the swirl Reynolds number increases, helical disturbances of the azimuthal wave number $m=1$ first become growing. This instability (being saturated to a finite-amplitude state) can induce bending and precession of the vortex (or swirling jet) axis observed in practical swirling flows.

ACKNOWLEDGMENT

The authors gratefully acknowledge the support of the Australian Research Council for the research.

[1] G. J. Nathan, S. J. Hill, and R. E. Luxton, J. Fluid Mech. **370**, 347 (1998).
[2] G. J. Nathan, R. E. Luxton, and J. P. Smart, *Proceedings of the Combustion Institute* (The Combustion Institute, 1992), Vol. 24, pp. 1399–1405.
[3] G. I. Taylor, Q. J. Mech. Appl. Math. **3**, 129 (1950).
[4] M. A. Goldshtik, J. Appl. Math. Mech. **24**, 610 (1960).
[5] J. Serrin, Philos. Trans. R. Soc. London, Ser. A **271**, 325 (1972).
[6] V. Shtern and F. Hussain, Annu. Rev. Fluid Mech. **31**, 537 (1999).
[7] J. C. Guilloud, J. Arnault, and C. Discrescendo, J. Mec. **12**, 471 (1973).
[8] M. A. Goldshtik and V. N. Shtern, J. Fluid Mech. **218**, 483 (1990).
[9] R. P. Davies-Jones, in *Thunderstorms: A Social, Scientific and Technological Documentary*, edited by K. Kessler (University of Oklahoma Press, Norman, 1983), Vol. 2.
[10] M. A. Goldshtik, Annu. Rev. Fluid Mech. **22**, 441 (1990).
[11] V. Shtern and F. Hussain, J. Fluid Mech. **309**, 1 (1996).
[12] V. Shtern and P. G. Drazin, Proc. R. Soc. London, Ser. A **456**, 1139 (2000).
[13] V. Shtern and F. Hussain, J. Fluid Mech. **480**, 283 (2003).
[14] M. V. Lowson, J. R. Aeronaut. Soc. **68**, 343 (1964).
[15] T. Sarpkaya, AIAA J. **9**, 1792 (1971).
[16] O. R. Burggraf and M. R. Foster, J. Fluid Mech. **80**, 685 (1977).
[17] L. Landau and E. M. Lifshitz, *Fluid Dynamics*, 2nd ed. (Pergamon, Oxford, 1987).
[18] M. Van Dyke, *Perturbation Methods in Fluid Mechanics* (Academic, New York, 1964).
[19] R. R. Long, J. Fluid Mech. **11**, 611 (1961).
[20] H. Schlichting, Z. Angew. Math. Mech. **13**, 260 (1933).
[21] V. Shtern and F. Hussain, J. Fluid Mech. **336**, 33 (1998).
[22] P. G. Drazin and W. H. Reid, *Hydrodynamic Stability* (Cambridge University Press, Cambridge, 1981).